RESEARCH ARTICLE

VIEW

On-demand field shaping for enhanced magnetic resonance imaging using an ultrathin reconfigurable metasurface

Hanwei Wang[1,2] | **Hsuan-Kai Huang**[1,2] | **Yun-Sheng Chen**[1,3] | **Yang Zhao**[1,2]

[1] Department of Electrical and Computer Engineering, University of Illinois at Urbana-Champaign, Urbana, Illinois, USA

[2] Holonyak Micro and Nanotechnology Laboratory, University of Illinois at Urbana-Champaign, Urbana, Illinois, USA

[3] Beckman Institute for Advanced Science and Technology, University of Illinois at Urbana-Champaign, Urbana, Illinois, USA

Correspondence
Yun-Sheng Chen and Yang Zhao, Department of Electrical and Computer Engineering, University of Illinois at Urbana-Champaign, Urbana, IL 61801, USA.
Email: yzhaoui@illinois.edu, yunsheng@illinois.edu

The signal-to-noise ratio (SNR) is the main figure of merit that assesses the quality of magnetic resonance imaging (MRI). Existing studies mainly focus on improving the magnetic field intensities of the constant homogenous B_0 field from the main coil or the oscillating B_1 field from the radio frequency (RF) coil. In addition to these options, SNR also depends on the coupling between the imaging subject and the RF coil during the signal reception, which has been largely ignored. Here, we provide a different route toward enhancing the SNR of MRI by improving this coupling during the signal reception. We elucidate a theoretical design of an ultrathin metasurface with micrometer thickness and high flexibility. This metasurface is reconfigurable; it can selectively boost the SNR at a desired imaging region with any arbitrary shapes. Our design has shown that this metasurface can enhance SNR by up to 28 times in the region of interest. At the same time, the metasurface is designed to minimally disturb the excitation fields by less than 1.6%, thus maintaining the uniformity of the excitation, important to achieve a high-quality MR image without artifacts.

KEYWORDS
magnetic resonance imaging, medical imaging instrumentation, metamaterials, reconfigurable

Magnetic resonance imaging (MRI) has been widely used in staging tumors, imaging musculoskeletal systems, and monitoring brain functions.[1,2] In MRI, the contrast among different types of tissue originates from the different decay rates of precession of nucleus spins.[3] The typical resolution of MRI is in micrometers, and the scanning time is about tens of minutes; both the resolution and the scanning time depend heavily on the signal-to-noise ratio (SNR) of the imaging area.[2] Therefore, the SNR has been a critical parameter associated with the imaging quality of MRI.

As the static magnetic B_0 field in MRI governs the magnetization of the nucleus spins, the signal increases with a stronger B_0 field intensity.[4] On the other hand, the noises of MRI include Johnson noise of the imaging subject, Larmor frequency shift due to subject-receiving coil induction, resistive noise of the receiving coil, and circuit noise of the preamplifier.[3] The major source of noises is Johnson noise caused by the Brownian motion of the electrons, which does not increase with the B_0 field intensity. As a result, when B_0 field increases from 3T to 7T, the SNR can be

enhanced by approximately 5.4 times. However, the safety of a strong magnetization on biological subjects remains unclear;[5] the financial cost to generate such a strong magnetic field is also substantial.[6]

Another approach to enhance SNR is to increase the oscillating B_0 field emitted and/or received by the receiving coil. Different surface coils have been designed for various imaging targets, such as eyes,[7] knees,[8] and heads.[9] While a specific designed surface coil can improve the SNR by 2.7^9–5^7 fold, it needs to be redesigned for different organs due to the constraints in shapes and rigidity; once developed, it does not provide the flexibility to image the specific region of interest within the imaging target. Recent research has shown great promise of applying the concept of metamaterials in MRI to further enhance the SNR without modifying the imaging system.[10,11–13] Metamaterials are subwavelength periodic structures that can achieve anomalous field effects that are not available in natural materials.[14] Because of the advantages of independently controlling the localized fields, metamaterials have been widely applied to boost or reshape electromagnetic fields in imaging applications.[15] Notably, a metamaterial consisting of an array of copper-wires has shown to enhance the SNR of MRI by 2.7 times[12] and a metamaterial with spiral arrays has shown to enhance the SNR by 4.2 times.[11] However, one remaining challenge of this concept is the nonuniformity of the excitation field caused by the metamaterials.

To enhance the signals at the receiving coil, while preserving the uniformity of the excitation field, metamaterials with nonlinearities[13] have been developed to tune the resonance frequencies, so it can be switched on/off during the reception/excitation.[13] The nonlinear metamaterial can enhance SNR up to 15.9 times without interrupting the excitation but requires a thickness over 5 cm, which creates challenges to fit in the limited space between the patient and the receiving coil.[9] Further enhancing the SNR based on this concept is limited because the energy is distributed in a large region. Very different from the previous work, here, we employ an ultrathin dynamically reconfigurable metasurface.[16] Although resonance tuning is also feasible with our metasurface design, our working principle does not rely on tuning the resonances, but rather on reforming the eigenmodes of the metasurface for an on-demand enhancement region. We show that a maximum 28-fold enhancement of the SNR in a user-defined area can be achieved, simultaneously overcoming the limitation of the spatial constraints with an ultrathin profile in micrometers.

In MRI, the RF coil generates an oscillating magnetic field B_0 to excite the proton-spin, and the decay is captured by the receiving coil. Here, we use B_1^+ and B_1^- to represent the excitation signal and the reception signal, respectively. Because metasurfaces/metamaterials are oftentimes

made of high-index dielectric materials or metal, it can locally enhance the electromagnetic fields but at the same time also create phase disruptions. The phase disruptions are not desired during the excitation, because it will create a nonuniform three-dimensional MR image as well as complicate the image reconstruction. To avoid phase disruptions during the excitation, we reform the eigenmodes of the metasurface only during the reception for an on-demand enhancement region, therefore, specifically enhance the B_1^- field without influencing the B_1^+ field to ensure a uniform and optimal excitation. As a result, the receiving coil can measure a stronger decay-signal and thus achieve an improved SNR in the resulting image. With the contribution of the metasurface, the excitation B_1^+ field becomes B_{1m}^+, and the reception B_1^- field becomes B_{1m}^-, which includes both the original $B_1^{+/-}$ field and the scattered field from the metasurface. The objective of this study is to achieve a high enhancement ratio of the SNR, defined as B_{1m}^-/B_1^-, at the same time, keep B_{1m}^+/B_1^+ as close to 1 as possible.

To shape a user-defined distribution of the B_{1m}^- field, we need to tailor the eigenmode of the metasurface. The eigenmode is described by the normalized distribution of a_n, $a_n = \sqrt{\frac{\hat{L}}{2}} I_n e^{i\omega_0 t}$, where $\hat{L}$ and I_n are the self-inductance and current of each unit cell. $\hat{L}$ is normalized as 1 H. ω_0 is the angular frequency of the B_1^+ and B_1^- field. Note that although the signal detected by the receiving coil B_1^- is generated by the imaging subject, based on the principle of reciprocity, the same field B_1^- can be generated by the receiving coil with a unit current at a specific location of the imaging subject. This concept is used to design our metasurface.

Our metasurface is composed of periodic arrays of resonators with significant mutual coupling among the neighboring unit cells. According to the coupled mode theory,[17] a_n is related to the coupling among the unit cells (κ_{kn}) of the metasurface, the intrinsic loss (Γ_n), and the driving force ($F_n(t)$) of each unit cell,

$$\frac{da_n(t)}{dt} = (i\omega_0 - \Gamma_n)a_n(t) + i\sum_{k=1}^{m}\kappa_{kn}a_k(t) + F_n(t), \quad (1)$$

where m is the total number of the unit cells of the metasurface. The intrinsic loss Γ_n is directly associated with the impedance Z_n of each unit cell as $\Gamma_n = \frac{Z_n}{2\hat{L}}$. κ_{kn} is the coupling coefficient between the kth and nth unit cell. The driving force, $F_n(t)$, excites the eigenmodes of the metasurface but does not define the eigenmodes; therefore, we ignore this term in our design.

By expanding Equation (1), we deduce the relation among the intrinsic loss Γ_n, the coupling coefficient κ_{kn},
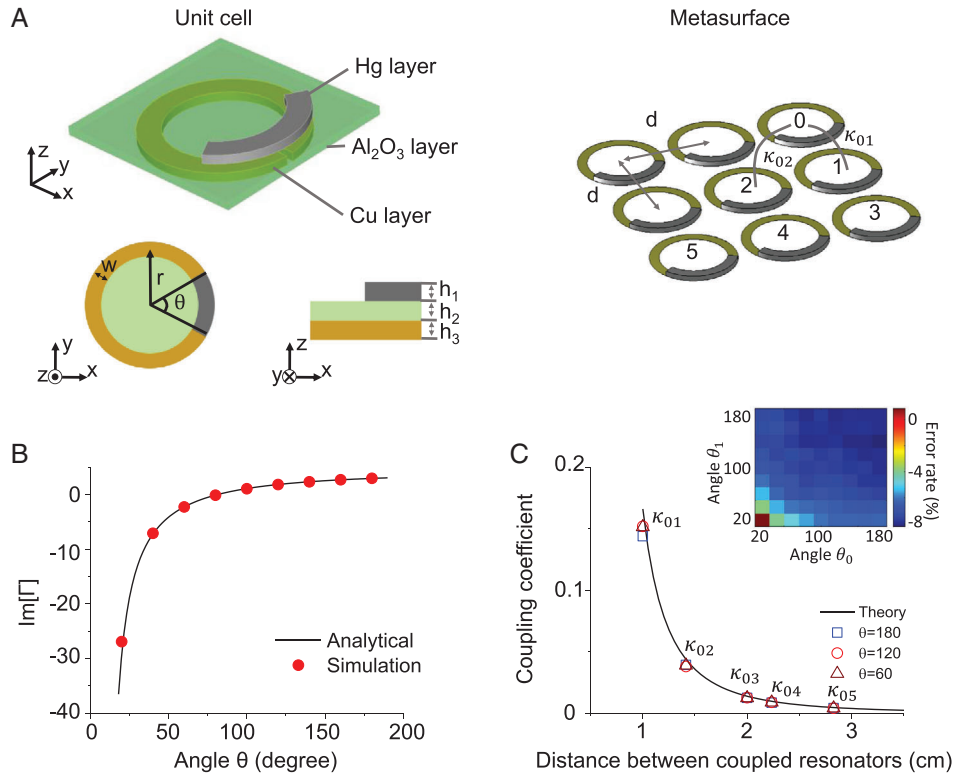
FIGURE 1 Configuration of the metasurface. (A) Left: The unit cell of the metasurface is composed of a Hg-Al$_2$O$_3$-Cu tri-layer structure with a capacitive layer in between the Hg and Cu layers. The capacitance can be tuned by the overlap area between the top and bottom layers. The radius r of the Hg and Cu rings is 4 mm, the width w is 1 mm, and the thickness h$_1$, h$_2$, and h$_3$ is 500, 1, and 1.2 μm, respectively. Right: Schematic illustration of a reconfigurable metasurface composed of 3 × 3 unit cells, d is the in-pane periodicity, κ_{01} refers to the coupling coefficient between the 0th and 1st unit cells. (B) Im[Γ] as a function of the arc angle (θ) of the Hg layer. The analytical results are calculated using the RLC lumped circuit element model. (C) Comparison between simulated and analytical coupling coefficients as a function of distance between coupled resonators by assuming the periodicity d of 1 cm. For example, κ_{01} denotes the coupling coefficient between the 0th and 1st unit cells as shown in (A). The inset shows the error map between simulated and analytical coupling coefficients with various angles θ for unit cell 0 and unit cell 1

and the targeting eigenmode a_{nt} (Supporting Information, Section I),

$$\Gamma_n = \frac{i \sum_{k=1}^{m} \kappa_{kn} a_{kt}}{a_{nt}}. \quad (2)$$

To shape the eigenmode, one can either tune the coupling coefficients κ_{kn} or the intrinsic loss Γ_n of each unit cell. As κ_{kn} depends on the relative positions of the unit cells, changing the position of one unit cell will alter its relative position to the rest of the unit cells. Therefore, κ_{kn} can hardly be controlled independently. On the other hand, Γ_n is only related to the impedance of each unit cell, thus, can be readily controlled independently. In our metasurface design, we fix the coupling coefficient κ_{kn} (i.e., the periodicity of the metasurface), and tune Γ_n to achieve the desired eigenmode. The real part of Γ represents the intrinsic resistive loss of the unit cell that leads to attenuation of the B_{1m}^- field, therefore, lossless/low-loss materials at the operation frequency needs to be employed for constructing the metasurface to minimize heating. The imaginary

part of Γ (Im[Γ_n]) comes from the capacitance and inductance of each unit cell constituting the metasurface, with the capacitance being the dominant variable at the given frequency. Therefore, we choose to tune the capacitance in our metasurface design.

Here, we focus on designing a metasurface operating at 127 MHz that corresponds to the magnetic resonance frequency of proton in the 3T MRI, as commonly used in current clinical scanner. As shown in Figure 1A, our metasurface is composed of a metal-insulator-metal tri-layer structure. The top layer is a microfluidic circular channel with a radius r. The channel is partially fill with a liquid metal (such as eutectic gallium–indium alloy or mercury) with an arc angle θ to form a C shaped metal layer. The additional liquid metal can be pumped in and out to change the arc angle θ, and thus tune the Im[Γ_n].[18] We chose mercury (Hg) as a model liquid metal to demonstrate our theory since its optical properties are well known. The spacer layer is aluminum oxide (Al$_2$O$_3$), and the bottom layer is a fixed Cu ring-resonator. The
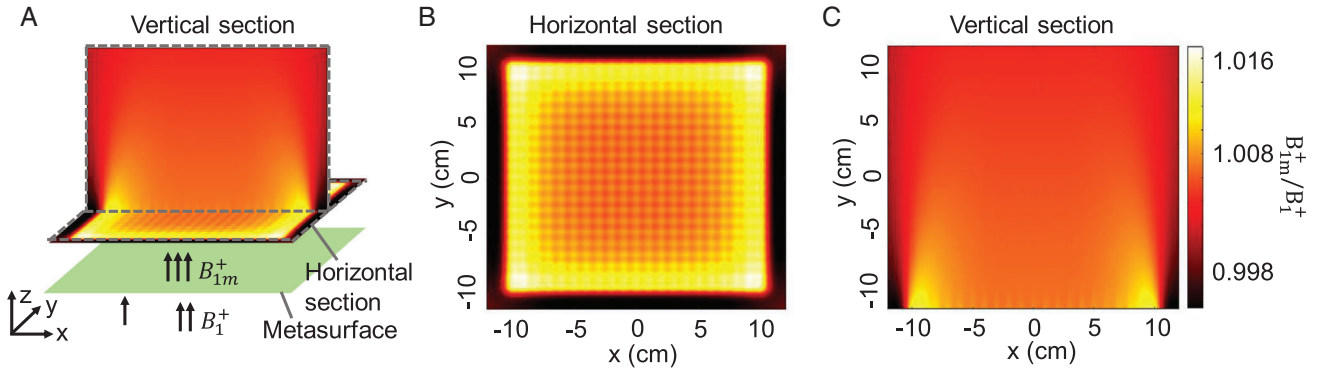
FIGURE 2 Excitation field when the impedance of the metasurface is tuned to minimally disturbing the field. (A) Magnetic field distribution with all 21×21 unit cells of the metasurface that are turned "off" to provide a uniform excitation. All θ are tuned to 20° so Im[Γ] at 127 MHz is –29.3. The feeding field is linearly polarized uniform magnetic field with the field direction vertical to the metasurface plane. B_1^+ and B_{1m}^+ are the excitation fields with and without the metasurface. (B) The excitation field in the horizontal cross-section at 1 cm above the metasurface. (C) The excitation field in the vertical cross-section as shown in (A)

periodicity (d) of the metasurface is 1 cm, the radius (r) is 4 mm, and the width (w) is 1 mm. The thickness of the top, spacer, and bottom layers of the metasurface (h_1, h_2, and h_3) is 500, 1, and 1.2 μm, respectively.

We first explore the relation between θ and Im[Γ] and simulate Im[Γ] as a function of various θ using the finite element method (CST studio suite 2019), and compare these results with analytical calculations. The analytical results (Figure 1B, black curve) are generated using the lumped circuit model. Our simulation matches well with the analytical solution with an error less than 1.35% (Figure 1B). To reduce the computational burden, we use the analytical solution in our later design. Our results show that as the arc angle θ changes from 20° to 180° (Figure 1B), Im[Γ] can be tuned from –29.3 (at 20°) to 2.94 (at 180°), sufficient to switch the desired eigenmode "off" and "on" during the excitation and reception.

There are two approaches to calculate the coupling coefficients κ_{kn} among each unit cells, one is the analytical approach based on Neumann's theory of mutual inductance, and the other is the full wave numerical simulation. The analytical approach is more computational efficient thus more readily adaptable in the field. Note that the Neumann's theory assumes the inductors' width is negligible comparing to their distances, so the analytical approach will lead to increasing errors when the distances between coupling unit cells reduce. We compare the analytical results of κ_{kn} with numerical simulations among six nearby unit cells (unit cells 0–5) by assuming the metasurface periodicity d = 1 cm (Figure 1C). As expected, when the distances between the coupling unit cells increase, the coupling coefficients κ_{kn} decay, and the absolute errors of the analytical results also decrease. When the distance between two unit cells is fixed (i.e., between unit cell 0 and unit cell 1), the error between the analytical result and the

simulation is dependent on the arc angle θ. The smaller the arc angle θ of each unit cell, the smaller the error will be.

A reconfigurable metasurface allows for selectively turning "off" and "on" the eigenmode in the excitation and reception of the MRI by changing the arc angle θ. During the excitation, a uniform B_{1m}^+ field distribution is desired, so we turn "off" the eigenmode of the metasurface by setting the angle θ of all unit cells at 20°. As shown in Figure 2, B_{1m}^+ field remains mostly uniform, and the difference between B_{1m}^+ field and B_1^+ field is less than 1.6%, demonstrating the minimal influence of the metasurface during the excitation.

During the reception, to enhance the B_{1m}^- field thus the SNR in a region of interest, we reset the Im[Γ] distribution to switch "on" the eigenmode. To demonstrate this on-demand regional enhancement, we choose a target region from a brain tumor MRI scan[19] as shown in Figure 3A. The goal is to create the enhanced B_{1m}^- field that matches the shape of the brain tumor and minimize the B_{1m}^- field elsewhere. To do so, ideally, the amplitude of the eigenmode a_{nt} outside the tumor region should be 0 and inside the tumor should be 1. However, the desired eigenmode distribution is formed by the entire field both outside and inside the region of interest. Therefore, if the field amplitude outside the tumor is set to be 0, one cannot achieve the desired enhancement inside the tumor region. We choose a target distribution with the field amplitude outside the tumor region to be 0.1, and inside the tumor to be 1.

To achieve a_{nt} as 1 for the tumor region and 0.1 elsewhere, we design the impedance map of the metasurface as shown in Figure 3B. Our calculation shows that the B_{1m}^-/B_1^- ratio can be enhanced 6.2 and 3.4 times, respectively, in the imaging planes at 1 and 2 cm above the metasurface (Figures 3C and D). Although the enhancement
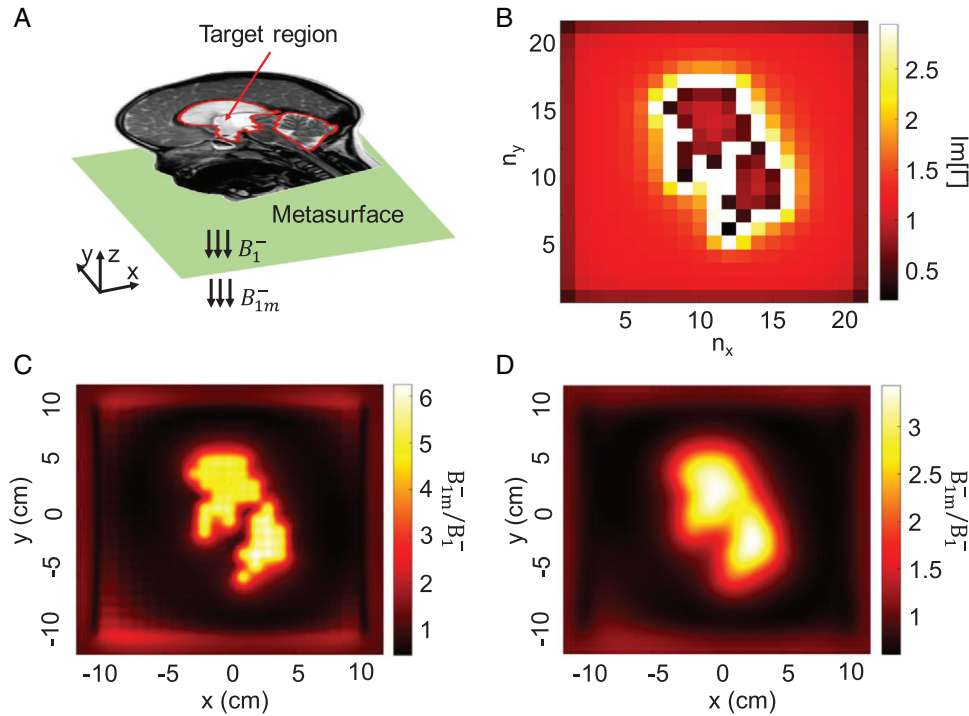
FIGURE 3 Metasurface for an on-demand enhancement region of a brain tumor. (A) Target magnetic field with enhancement region of a brain tumor. B_1^- and B_{1m}^- are the reception fields with and without the metasurface. Both B_1^- and B_{1m}^- are linearly polarized along the z-direction. The MRI brain tumor image is adapted from Ref.[19]. (B) Calculated Im[Γ] distribution, where all Im[Γ] exceed 2.94 are set as 2.94. (C and D) Horizontal section of the overall magnetic field at 1 and 2 cm above the metasurface. The MR image is reproduced from Ref.[19]. Copyright 2020, ISPN guidance to pediatric neurosurgery

ratio decays gradually as the imaging plane moves away from the metasurface, the enhancement ratio remains at least 1.5 times at 5 cm above the metasurface.

Because of energy conservation, the enhancement ratio inevitably decays. By taking advantage of the reconfiguration of the metasurface, it is possible to redirect the energy and extend the enhancement region further with the cost of a relatively smaller enhancement ratio near the metasurface. This can be achieved by selectively "focusing" the field with a metasurface supporting nonuniform eigenmode, such as a Gaussian distribution. The intensity distribution of a Gaussian field is

$$I(x, y) = \exp\left(-\frac{4\ln(2)\sqrt{(x-x_0)^2 + (y-y_0)^2}}{w^2}\right), \quad (3)$$

where w is the full width at half maximum (FWHM), x_0 and y_0 are the coordinates of the "focal point." Figures 4A and C show various Im[Γ] distributions of the metasurface, which targets a Gaussian eigenmode with an FWHM of 4 and 8 cm, respectively, with a focus location at (0 cm, 0 cm). When translating the Im[Γ] distribution, we can move the "focal point" in the transverse plane as seen in

Figure 4B, where the 4 cm-FWHM enhancement region is relocated to (0 cm, 4 cm).

The enhancement ratio at the focus depends on the FWHM of the field. We calculate the enhancement ratios of Gaussian fields with FWHM of 2, 4, 8, and 12 cm at various distances away from the metasurface to mimic the imaging penetration. As shown in Figure 4G, at a distance of 5 mm, the enhancement ratio at the "focal point" of 2 cm-FWHM-Gaussian field is 28; for 4-, 8-, and 12 cm-fields, the enhancement ratios are 21, 15, and 12, respectively, which is 2–11 fold higher compared to other metamaterial designs at the same imaging depth. At such a distance, the enhancement ratio of a 2 cm-Gaussian field is shown to be 28 at the center of the field. Using this typical distance between the metasurface/metamaterial and the imaging subject, the enhancement ratio of the wire-metasurface is ~2.5;[20] the magnetic metamaterials is ~4;[11] and the nonlinear magnetic metamaterials is ~16.[13]

As seen in Figure 4G, the decay rate of the signals along the z-direction is related to the designed FWHM of the Gaussian field. A broader targeted field will lead to a slower decay rate but a lower initial intensity right above the metasurface, because the energy is distributed to a larger area. To optimize the enhancement ratio at a certain depth z, one can choose the field-width by considering both the
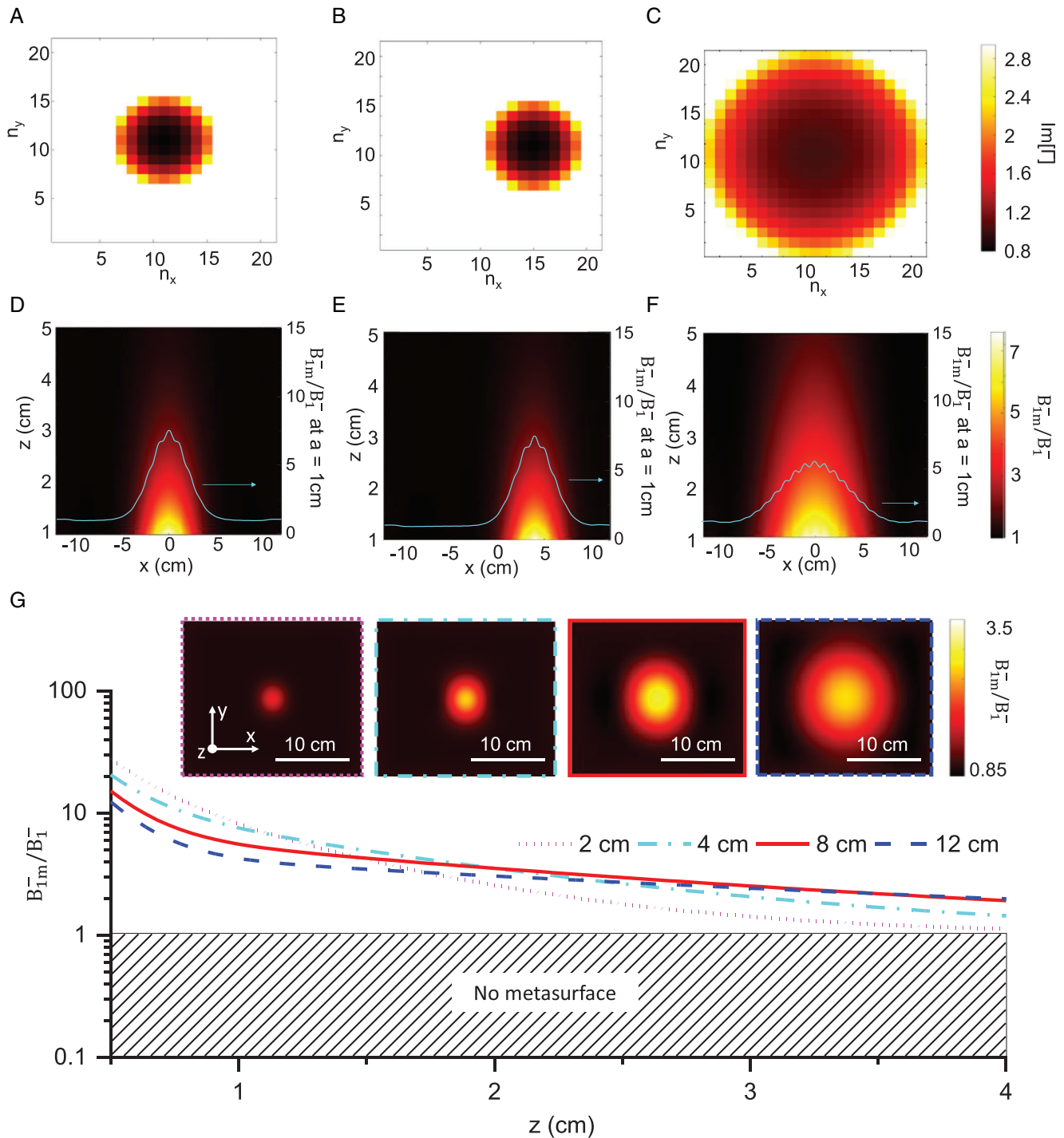
FIGURE 4 Gaussian field with controllable field-width and position. (A)–(C) Im[Γ] distribution of a Gaussian field with field-width of 4, 4, and 8 cm and central location of (0 cm, 0 cm), (4 cm, 0 cm), and (0 cm, 0 cm), respectively. (D)–(F) The vertical cross-section (x–z plane) of the magnetic field with 1 cm above the metasurface corresponding to (A)–(C). The blue curves represent the enhancement ratio at z = 1 cm. (G) Enhancement ratio at the focal point as a function of z for 2-, 4-, 8-, and 12 cm-FWHM Gaussian field. The insets show x–y cross-section at 2.5 cm above the metasurface of the four Gaussian field, respectively

initial value and the decay rate. As compared in Figure 4G, at 2.5 cm above the metasurface, the 8 cm-Gaussian field can achieve a relatively higher enhancement ratio than the 4 cm-Gaussian field by 12.17% due to its slower field decay, and a higher enhancement ratio than 12 cm-Gaussian field by 9.49% due to its higher initial intensity. In this way, one can control the desired SNR-enhanced region in three dimensions.

In many scenarios, the imaging region is not close to the surface of the subject. To receive the signal with a
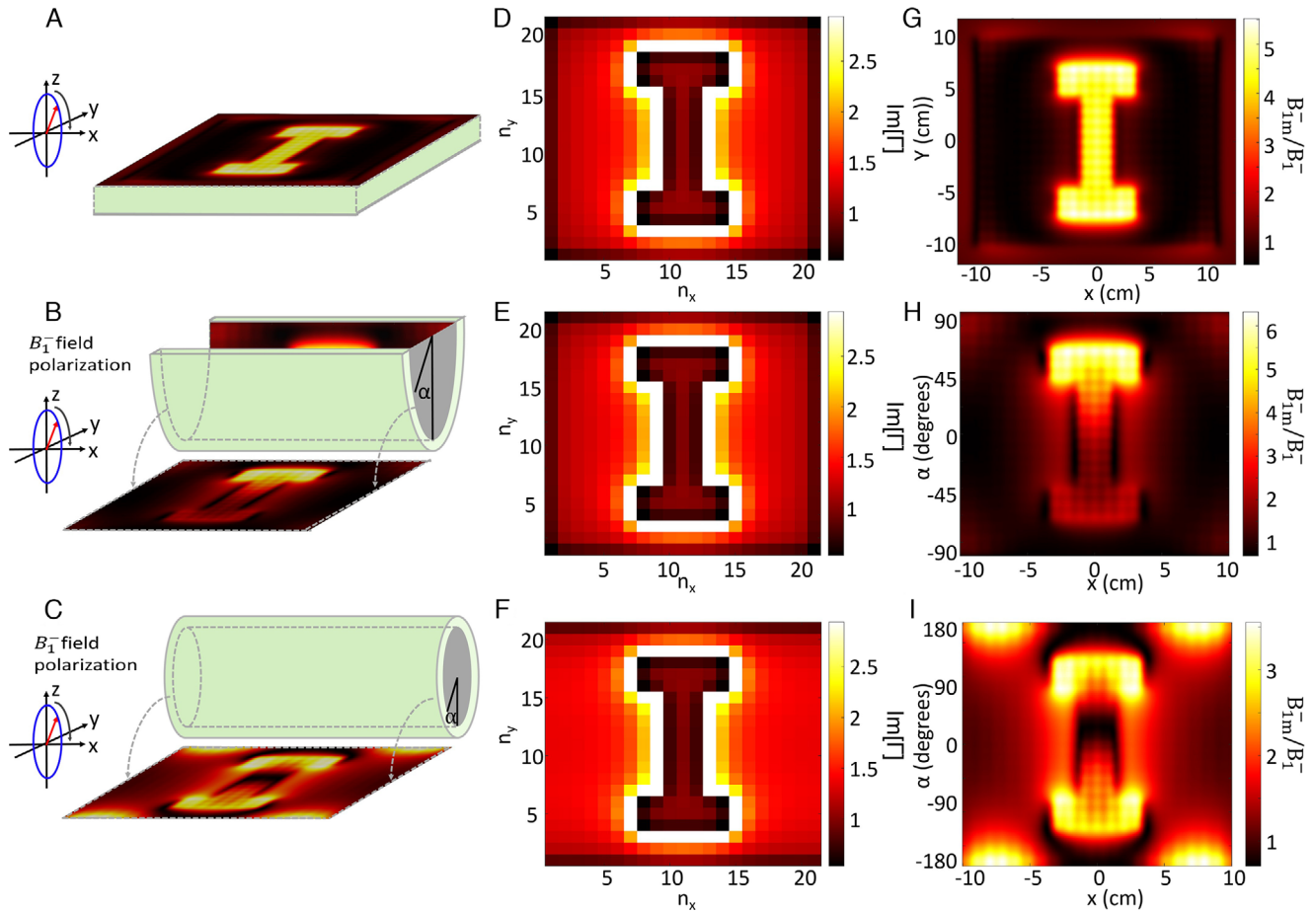
FIGURE 5 Cylindrical metasurface to meet the need of curved imaging subjects. (A)–(C) Schematic illustrations of metasurfaces with different curvature: (A) planar, (B) half-cylindrical, and (C) cylindrical. The B_1^- field is circularly polarized (left handed) with the field vector rotating on the yz-plane. The targeted eigenmode is designed as a letter "I" shape. The observation plane is at 1 cm above the metasurface. (D)–(F) Corresponding impedance distribution that will generate the target eigenmodes. (G)–(I) Field distribution on the observation plane

lower attenuation in depth, the RF coil is often chosen as a birdcage coil instead of a surface coil.[8] The excitation field is circularly polarized instead of linearly polarized, and the gap between the coil and the subject is cylindrical. As Al_2O_3 becomes flexible with micrometer thickness,[21] the metasurface can be bendable and fit into the curved gap between the birdcage coil and the imaging subject. To test the performance of the metasurface with different bending curvature and circularly polarized B_1^- field, we simulate a planar, half-cylindrical, and cylindrical metasurface as shown in Figures 5A–C to achieve a desired imaging area that shapes as the letter "I." Figures 5D and E show the calculated $Im[\Gamma]$ map of the metasurface that remains relatively unchanged across the three different curvatures. It is because for certain targeted eigenmodes, $Im[\Gamma]$ is mostly determined by the coupling coefficient (κ) between the neighboring unit cells; the unit cell is much smaller than the metasurface with each taking only 0.23% of the area, so the coupling coefficient between the neighboring unit cells is insensitive to the curvature.[22] The imag-

inary part of Γ_n is much larger than its real part, as shown in Equation (3), the eigenmode of the metasurface can only be linearly polarized (a_{nt} needs to be in-phase). On the other hand, the B_1^- field is circularly polarized (left handed), which mismatches with the eigenmode polarization. This mismatch results in the distortion of B_{1m}^- field as shown in Figures 5G–I, which increases with the curvature of the metasurface. Moreover, as the shape "I" is nonuniformly distributed among the rotational angle α, the B_{1m}^-/B_1^- field is asymmetric with respect to α, this relationship will be reversed with an opposite handedness B_1^-. Despite the distortion induced by the polarization mismatch, the enhancement ratio at a certain part of the "I" shape remains high. So, the selective enhancement is still achievable for the scenarios using a birdcage coil.

In summary, here we introduced a design of reconfigurable metasurface for enhancing the receiving imaging signals on demand. In our demonstration, we have assumed a 3T B_0 field MRI, our design principle can be extended to other static B_0 fields by slightly changing the

unit cell parameters. Our designed metasurface can boost the reception fields, while poses little disruption to the excitation fields; notably, the designed enhancement ratio in a 3T-MRI is up to 28 times, while the disturbance of the excitation field is less than 1.6% across various imaging depth. These results demonstrate that we can achieve an on-demand enhancement in the MR images without the need of increasing the local magnetic fields. By shaping the uniformity of the enhancement region, we also show the tunability of the decay rate of the enhanced field across various imaging depths, highlighting the flexibility in enhancing MR imaging in three dimensions.

CONFLICT OF INTEREST

The authors declare no conflict of interest.

ORCID

Yang Zhao https://orcid.org/0000-0002-0154-3483

REFERENCES

1. a) S. Ogawa, T. M. Lee, A. R. Kay, D. W. Tank, *Proc. Natl. Acad. Sci. USA* **1990**, *87*, 9868; b) D. Weishaupt, V. D. Köchli, B. Marincek, *How does MRI Work? An Introduction to the Physics and Function of Magnetic Resonance Imaging*, Springer Science & Business Media, **2006**; c) R. W. Brown, Y.-C. N. Cheng, E. M. Haacke, M. R. Thompson, R. Venkatesan, *Magnetic Resonance Imaging: Physical Principles and Sequence Design*, Wiley-Blackwell, **2014**; d) N. Petridou, D. Plenz, A. C. Silva, M. Loew, J. Bodurka, P. A. Bandettini, *Proc. Natl. Acad. Sci. USA* **2006**, *103*, 16015; e) J. Duyn, A. P. Koretsky, *Nat. Clin. Pract. Cardiovasc. Med.* **2008**, *5*, S71; f) A. Barandov, B. B. Bartelle, C. G. Williamson, E. S. Loucks, S. J. Lippard, A. Jasanoff, *Nat. Commun.* **2019**, *10*, 897.

2. Z.-P. Liang, P. C. Lauterbur, *Principles of Magnetic Resonance Imaging: A Signal Processing Perspective*, SPIE Optical Engineering Press, **2000**.

3. D. G. Nishimura, *Principles of Magnetic Resonance Imaging*, Stanford University, **2010**.

4. V. D. Schepkin, F. C. Bejarano, T. Morgan, S. Gower-Winter, M. Ozambela Jr., C. W. Levenson, *Magn. Reson. Med.* **2012**, *67*, 1159.

5. V. Hartwig, G. Giovannetti, N. Vanello, M. Lombardi, L. Landini, S. Simi, *Int J Environ Res Public Health* **2009**, *6*, 1778.

6. A. Nowogrodzki, *Nature* **2018**, *563*, 24.

7. F. Schenck, A. Hart, H. Foster, A. Edelstein, A. Bottomley, W. Redington, *American Journal of Roentgenology* **1985**, *144*, 5.

8. D. Burk, E. Kanal, J. Brunberg, G. Johnstone, H. Swensen, G. Wolf, *Am. J. Roentgenol.* **1986**, *147*, 293.

9. J. A. d. Zwart, P. J. Ledden, P. Kellman, P. v. Gelderen, J. H. Duyn, *Magn. Reson. Med.* **2002**, *47*, 1218.

10. a) A. Hurshkainen, A. Nikulin, E. Georget, B. Larrat, D. Berrahou, A. L. Neves, P. Sabouroux, S. Enoch, I. Melchakova, P.

Belov, S. Glybovski, R. Abdeddaim, *Sci. Rep.* **2018**, *8*, 9190; b) E. I. Kretov, A. V. Shchelokova, A. P. Slobozhanyuk, *Appl. Phys. Lett.* **2019**, *115*, 061604; c) R. Schmidt, A. Slobozhanyuk, P. Belov, A. Webb, *Sci. Rep.* **2017**, *7*, 1678; d) R. Schmidt, A. Webb, *ACS Appl. Mater. Interfaces* **2017**, *9*, 34618; e) A. V. Shchelokova, A. P. Slobozhanyuk, S. Saha, I. Sotiriou, M. Koutsoupidou, G. Palikaras, E. Kallos, P. A. Belov, A. Webb, "In vivo magnetic resonance imaging of human knee with metasurface", presented at *2017 Progress in Electromagnetics Research Symposium - Spring (PIERS)*, **2017**.

11. G. Duan, X. Zhao, S. W. Anderson, X. Zhang, *Commun. Phys.* **2019**, *2*, 35.

12. A. P. Slobozhanyuk, A. N. Poddubny, A. J. E. Raaijmakers, C. A. T. v. d. Berg, A. V. Kozachenko, I. A. Dubrovina, I. V. Melchakova, Y. S. Kivshar, P. A. Belov, *Adv. Mater.* **2016**, *28*, 1832.

13. X. Zhao, G. Duan, K. Wu, S. W. Anderson, X. Zhang, *Adv. Mater.*, **2019**, *31*, 1905461.

14. a) R. A. Shelby, D. R. Smith, S. Schultz, *Science* **2001**, *292*, 77; b) J. B. Pendry, D. Schurig, D. R. Smith, *Science* **2006**, *312*, 1780; c) J. Valentine, S. Zhang, T. Zentgraf, E. Ulin-Avila, D. A. Genov, G. Bartal, X. Zhang, *Nature* **2008**, *455*, 376; d) N. I. Zheludev, Y. S. Kivshar, *Nat. Mater.* **2012**, *11*, 917; e) A. Boltasseva, H. A. Atwater, *Science* **2011**, *331*, 290; f) S. Linden, C. Enkrich, M. Wegener, J. Zhou, T. Koschny, C. M. Soukoulis, *Science* **2004**, *306*, 1351; g) O. Hess, J. B. Pendry, S. A. Maier, R. F. Oulton, J. M. Hamm, K. L. Tsakmakidis, *Nat. Mater.* **2012**, *11*, 573; h) A. Alù, M. G. Silveirinha, A. Salandrino, N. Engheta, *Phys. Rev. B* **2007**, *75*, 155410; i) Y. Zhao, M. A. Belkin, A. Alù, *Nat. Commun.* **2012**, *3*, 870; j) N. Engheta, R. W. Ziolkowski, *Metamaterials: Physics and Engineering Explorations*, John Wiley & Sons, Inc., Hoboken, NJ **2006**; k) N. Mohammadi Estakhri, B. Edwards, N. Engheta, *Science* **2019**, *363*, 1333; l) B. Luk'yanchuk, N. I. Zheludev, S. A. Maier, N. J. Halas, P. Nordlander, H. Giessen, C. T. Chong, *Nat. Mater.* **2010**, *9*, 707; m) N. Liu, H. Guo, L. Fu, S. Kaiser, H. Schweizer, H. Giessen, *Nat. Mater.* **2008**, *7*, 31; n) W. Cai, U. K. Chettiar, A. V. Kildishev, V. M. Shalaev, *Nat. Photonics* **2007**, *1*, 224; o) H. Alaeian, J. A. Dionne, *Phys. Rev. A* **2014**, *89*, 033829.

15. a) C. M. Soukoulis, M. Wegener, *Nat. Photonics* **2011**, *5*, 523; b) W. Fan, B. Yan, Z. Wang, L. Wu, *Sci. Adv.* **2016**, *2*, e1600901; c) Z. Jacob, L. V. Alekseyev, E. Narimanov, *Opt. Express*, **2006**, *14*, 8247; d) X. Zhang, Z. W. Liu, *Nat. Mater.* **2008**, *7*, 435; e) A. Poddubny, I. Iorsh, P. Belov, Y. Kivshar, *Nat. Photonics* **2013**, *7*, 948; f) C. M. Soukoulis, S. Linden, M. Wegener, *Science* **2007**, *315*, 47; g) Smolyaninov, II, Y. J. Hung, C. C. Davis, *Science* **2007**, *315*, 1699; h) J. Zhu, J. Christensen, J. Jung, L. Martin-Moreno, X. Yin, L. Fok, X. Zhang, F. J. Garcia-Vidal, *Nat. Phys.* **2011**, *7*, 52; i) M. Khorasaninejad, F. Capasso, *Science* **2017**, *358*, eaam8100; j) N. Yu, F. Capasso, *Nat. Mater.* **2014**, *13*, 139; k) F. Aieta, P. Genevet, M. A. Kats, N. F. Yu, R. Blanchard, Z. Gahurro, F. Capasso, *Nano Lett.* **2012**, *12*, 4932.

16. a) A. V. Kildishev, A. Boltasseva, V. M. Shalaev, *Science* **2013**. *339*, 1232009; b) G. X. Zheng, H. Muhlenbernd, M. Kenney, G. X. Li, T. Zentgraf, S. Zhang, *Nat. Nanotechnol.* **2015**, *10*, 308; c) C. L. Holloway, E. F. Kuester, J. A. Gordon, J. O. Hara, J. Booth, D. R. Smith, *IEEE Antennas Propag. Mag.* **2012**, *54*, 10; d) Y. Zhao, X. X. Liu, A. Alu, *J. Opt.* **2014**, *16*, 123001; e) H. T. Chen, A. J. Taylor, N. F. Yu, *Rep. Prog. Phys.* **2016**. *79*, 076401; f) Q. He, S. Sun, L. Zhou, *Research* **2019**, *2019*, 16; g) W. Zhang, Q. Song, W. Zhu, Z. Shen, P. Chong, D. P. Tsai, C. Qiu, A. Q. Liu, *Adv. Phys. X*,

2018, *3*, 1417055; h) W. Zhu, Q. Song, L. Yan, W. Zhang, P.-C. Wu, L. K. Chin, H. Cai, D. P. Tsai, Z. X. Shen, T. W. Deng, S. K. Ting, Y. Gu, G. Q. Lo, D. L. Kwong, Z. C. Yang, R. Huang, A.-Q. Liu, N. Zheludev, *Adv. Mater.* **2015**, *27*, 4665; i) Y. Hui, J. S. Gomez-Diaz, Z. Qian, A. Alù, M. Rinaldi, *Nat. Commun.* **2016**, *7*, 11249.

17. a) A. Kurs, A. Karalis, R. Moffatt, J. D. Joannopoulos, P. Fisher, M. Soljačić, *Science* **2007**, *317*, 83; b) H. A. Haus, W. Huang, *Proc. IEEE* **1991**, *79*, 1505.

18. P. C. Wu, W. Zhu, Z. X. Shen, P. H. J. Chong, W. Ser, D. P. Tsai, A.-Q. Liu, *Adv. Opt. Mater.* **2017**, *5*, 1600938.

19. *The ISPN Guide to Pediatric Neurosurgery*, **2020**.

20. R. Schmidt, A. Slobozhanyuk, P. Belov, A. Webb, *Sci. Rep.* **2017**, *7*, 1.

21. N. Münzenrieder, L. Petti, C. Zysset, T. Kinkeldei, G. A. Salvatore, G. Tröster, *IEEE Trans. Electron Devices* **2013**, *60*, 2815.

22. A. D. Falco, Y. Zhao, A. Alú, *Appl. Phys. Lett.* **2011**, *99*, 163110.

SUPPORTING INFORMATION

Additional supporting information may be found online in the Supporting Information section at the end of the article.